

# Multi-Contact Inertial Parameters Estimation and Localization in Legged Robots

Sergi Martinez<sup>1</sup> Robert J. Griffin<sup>2</sup> Carlos Mastalli<sup>1,2</sup>

**Abstract**—Optimal estimation is a promising tool for estimation of payloads’ inertial parameters and localization of robots in the presence of multiple contacts. To harness its advantages in robotics, it is crucial to solve these large and challenging optimization problems efficiently. To tackle this, we (i) develop a multiple shooting solver that exploits both temporal and parametric structures through a parametrized Riccati recursion. Additionally, we (ii) propose an *inertial manifold* that ensures the full physical consistency of inertial parameters and enhances convergence. To handle its manifold singularities, we (iii) introduce a nullspace approach in our optimal estimation solver. Finally, we (iv) develop the analytical derivatives of contact dynamics for both inertial parametrizations. Our framework can successfully solve estimation problems for complex maneuvers such as brachiation in humanoids, achieving higher accuracy than conventional least squares approaches. We demonstrate its numerical capabilities across various robotics tasks and its benefits in experimental trials with the Go1 robot.

## I. INTRODUCTION

OPTIMAL ESTIMATION (OE) [1] emerges as a powerful tool for interpreting observations and accurately estimating a system’s true state, including internal changes like unknown payloads. In the context of robotics, this framework takes into account both proprioceptive and exteroceptive observations [2], [3]. It systematically incorporates considerations such as robot dynamics and nonholonomics [4], balance conditions [5], and kinematic range. Its application in robotics holds promising potentials. For instance, it can be applied to estimate external parameters, e.g., aerodynamics effects in aerial navigation or internal parameters, e.g., unknown payloads as shown in Fig. 1.

Algorithms for optimal estimation solve variations of the following problem:

$$\begin{aligned} \min_{\mathbf{x}_s, \mathbf{w}_s, \boldsymbol{\theta}} & \frac{1}{2} \|\mathbf{x}_0 \ominus \bar{\mathbf{x}}_0\|_{\Sigma_{\mathbf{x}_0}^{-1}}^2 + \frac{1}{2} \|\boldsymbol{\theta} - \bar{\boldsymbol{\theta}}\|_{\Sigma_{\boldsymbol{\theta}}^{-1}}^2 \\ & + \frac{1}{2} \sum_{k=0}^{N-1} \|\mathbf{w}_k\|_{\Sigma_{\mathbf{w}_k}^{-1}}^2 + \frac{1}{2} \sum_{j=1}^N \|\hat{\mathbf{z}}_j \ominus \mathbf{h}(\mathbf{x}_j; \boldsymbol{\theta} | \hat{\mathbf{u}}_j)\|_{\Sigma_{\hat{\mathbf{z}}_j}^{-1}}^2 \\ \text{s.t.} & \quad \mathbf{x}_{k+1} = \mathbf{f}(\mathbf{x}_k; \boldsymbol{\theta} | \hat{\mathbf{u}}_k) \oplus \mathbf{w}_k, \quad \mathbf{x}_N = \mathbf{x}_{N-1}, \quad (1) \end{aligned}$$

where  $\mathbf{x} \in \mathcal{X} \subseteq \mathbb{R}^{n_x}$  represents the system’s state,  $\mathbf{w} \in \mathcal{T}_{\mathbf{x}} \mathcal{X} \subseteq \mathbb{R}^{n_x}$  describes its uncertainty,  $\boldsymbol{\theta} \in \mathbb{R}^{n_{\theta}}$  are static parameters defining the system’s inertial properties,  $\hat{\mathbf{u}}_k$  denotes the applied (and known) control commands (e.g., joint torques),  $\hat{\mathbf{z}} \in \mathcal{Z} \subseteq \mathbb{R}^{n_z}$  are observations, and  $\mathbf{x}_0$  is the arrival state. Eq. (1) finds the *maximum a-posteriori estimate*  $P(\mathbf{x}_s, \mathbf{w}_s, \boldsymbol{\theta} | \hat{\mathbf{z}}_s)$  as the state, parameters, uncertainties,

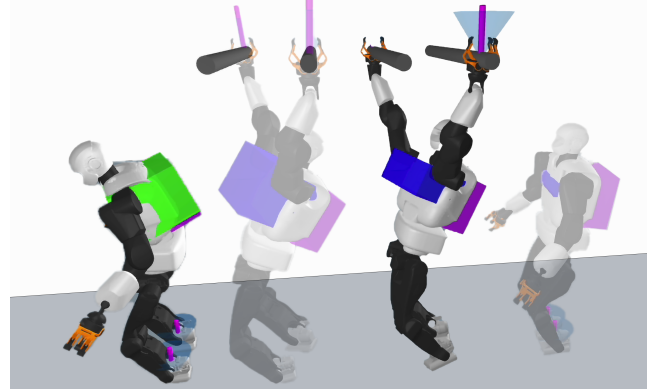


Fig. 1: Talos executing intricate monkey bar maneuvers with an unidentified payload. In the initial stages, our estimator meticulously pinpoints Talos’ localization and estimates its payload’s properties: mass, barycenter, and rotational inertia. The boxes’ sizes, positions, shape, and colors serve as visual indicators, representing estimations of the payload’s mass, barycenter, principal components of inertia, and algorithm convergence. To watch the video, click the picture or see [https://youtu.be/nDOxTgeK\\_5o](https://youtu.be/nDOxTgeK_5o).

and observations correspond to Gaussian distributions, i.e.,  $\mathbf{x}_k \sim \mathcal{N}(\bar{\mathbf{x}}_k, \Sigma_{\mathbf{x}_k})$ ,  $\boldsymbol{\theta} \sim \mathcal{N}(\bar{\boldsymbol{\theta}}, \Sigma_{\boldsymbol{\theta}})$ ,  $\mathbf{w}_k \sim \mathcal{N}(\mathbf{0}, \Sigma_{\mathbf{w}_k})$ , and  $\hat{\mathbf{z}}_k \sim \mathcal{N}(\mathbf{0}, \Sigma_{\hat{\mathbf{z}}_k})$ , respectively. The term  $\frac{1}{2} \|\mathbf{x}_0 \ominus \bar{\mathbf{x}}_0\|_{\Sigma_{\mathbf{x}_0}^{-1}}^2$  describes the *arrival state distribution*, where  $\ominus$  is the *difference operator* used to optimize over state manifolds [6], [7], [8]. Additionally, the term  $\frac{1}{2} \|\boldsymbol{\theta} - \bar{\boldsymbol{\theta}}\|_{\Sigma_{\boldsymbol{\theta}}^{-1}}^2$  specifies the uncertainties in the system’s parameters. Finally,  $\mathbf{f} : \mathcal{X} \times \mathbb{R}^{n_{\theta}} \rightarrow \mathcal{T}_{\mathbf{x}} \mathcal{X}$  and  $\mathbf{h} : \mathcal{X} \times \mathbb{R}^{n_{\theta}} \rightarrow \mathcal{Z}$  are nonlinear functions describing the robot dynamics and measurements. The observation set  $\hat{\mathbf{z}} \in \mathcal{Z}$  depends on the onboard sensors available on a robot. For example, in legged robots, this typically includes  $\hat{\mathbf{z}} = [\hat{\mathbf{q}}_j \ \hat{\mathbf{v}}_j \ \hat{\mathbf{q}}_i \ \hat{\omega}_i \ \hat{\lambda}_c]^T$ , where  $\hat{\mathbf{q}}_j$  and  $\hat{\mathbf{v}}_j$  are the joint positions and velocities,  $\hat{\mathbf{q}} \in \mathbb{R}^3$  and  $\hat{\omega} \in \mathbb{R}^3$  are the IMU linear accelerations and angular velocities, and  $\hat{\lambda}_c$  are the contact forces used to define the contact constraints.

### A. Related work

To address optimal estimation in robotics, one can leverage well-established *direct methods* [9], which transcribes Eq. (1) into a nonlinear programming (NLP) problem. Direct methods involve the discretization of both state and uncertainties, followed by optimization using sparse general-purpose NLP software such as SNOPT [10], KNITRO [11], and IPOPT [12]. These software rely on sparse linear solvers such as MA27, MA57, and MA97 (see [13]) to factorize the large Karush-Kuhn-Tucker (KKT) problem. However, a limitation of these linear solvers is their inefficiency in exploiting the Markovian structure of optimal estimation (OE) problems [14], restricting their applicability in real-time applications, especially in

<sup>1</sup> Robot Motor Intelligence (RoMI) Lab – Heriot-Watt University, UK.

<sup>2</sup> IHMC Robotics – Florida Institute for Human & Machine Cognition, US.

legged robotics. These computational limitations are attributed to their difficulties in utilizing data cache accesses efficiently, resulting in the exclusion of OE strategies. Indeed, recent works focused on factor graphs formulations with robot kinematics [15], [16], [17] are restricted to localization approaches only, ignoring the robot’s dynamics. In contrast, our approach considers the robot’s dynamics, thereby reducing drift errors in *proprioceptive localization* (see Fig. 5-bottom).

Alternatively, we can leverage Bellman’s principle of optimality [18] to break the optimal estimation problem into a sequence of smaller subproblems. This approach effectively exploits the Markovian structure, resulting in a differential dynamic programming (DDP) approach for optimal estimation [19]. Additionally, by augmenting the system’s state with its internal parameters, or parametrizing the dynamics, we can simultaneously solve identification and localization problems via DDP [20]. However, these DDP approaches, being *single shooting* algorithms, are prone to numerical instability and require a good initialization [9], both crucial considerations for their application in robotics. These numerical instabilities, arise from enforcing dynamic feasibility, can be mitigated through *feasibility-driven* methods [14], [21] or *multiple-shooting* strategies [22] as proposed in model predictive control (MPC) literature. Moreover, DDP approaches for optimal estimation presuppose knowledge of the *arrival state*, a condition not attainable in real-world applications. In contrast, our framework incorporates the *arrival state estimation*.

To estimate inertial parameters in robotics, two key aspects must be leveraged: (i) the affine relationship between these parameters and the generalized torques, as initially developed in [23], and (ii) the analytical derivatives of rigid body algorithms [24], [25]. The second aspect is particularly relevant to us, as the derivatives of forward dynamics rely on the inertial matrix method (IMM) outlined in [26]. This is because IMMs involve Cholesky decompositions of the joint-space inertia matrix, limiting their operation to inertial parameters that are *fully physically consistent*.

Conditions for full physical consistency boils down to triangle inequality constraints [27]. However, numerical optimization guarantees inequality feasibilities at convergence, limiting its application to IMMs. Alternatively, these conditions can be embedded in a smooth manifold defined via a log-Cholesky parametrization [28]. This manifold, being singularity-free, exhibits highly nonlinear geometry. Alternatively, it is possible to build a smoother manifold by developing an OE solver that handles these singularities. These ideas lead us to a novel *exponential eigenvalue manifold*, with a better convergence rate, coupled with a nullspace resolution (see Fig. 3).

## B. Contribution

Our main contribution is an efficient approach for solving hybrid optimal estimation problems in inertial identification and localization. It relies on three technical contributions:

- (i) a novel smooth manifold that guarantees full physical consistency of inertial parameters (Section III-B),
- (ii) analytical derivatives of the hybrid contact dynamics regarding the inertial parameters (Section IV), and

- (iii) a novel optimal estimation solver that handles singularities in inertial identification, arrival state estimation, and incorporates multiple shooting rollouts (Section V).

Our optimal estimation framework is the first of its kind and integrates the state-of-the-art log-Cholesky parametrization. This is because current frameworks (e.g., [28]) focuses solely on inertial identification via a *maximum likelihood approach*. Additionally, we develop a novel multiple shooting solver that combines nullspace parametrization to handle the exponential eigenvalue singularities. Such singularities occur when the principal components of inertia at barycenter are the same, as in a solid sphere or a disk with uniform density.

The article is structured as follows: Section II introduces contact dynamics, inertial parameters, and their conditions to physical consistency. To satisfy these conditions, Section III derives our exponential eigenvalue parametrization. Section IV describes the optimal estimation problem. Section V covers technical details of our optimal estimation solver: the parametrized Riccati recursion, multiple shooting rollouts, and arrival state estimation. Section VI presents results that demonstrate the benefits of our approach, while, Section VII provides the conclusion.

## II. BACKGROUND

### A. Contact dynamics

The dynamics of rigid body systems, subject to holonomic contact constraints at the acceleration level, are governed by:

$$\mathbf{M}(\mathbf{q})\dot{\mathbf{v}} = \boldsymbol{\tau}(\mathbf{u}) - \mathbf{h}(\mathbf{q}, \mathbf{v}) + \mathbf{J}_c(\mathbf{q})^\top \boldsymbol{\lambda}_c, \quad (2)$$

$$\mathbf{J}_c(\mathbf{q})\dot{\mathbf{v}} = -\mathbf{a}_c(\mathbf{q}, \mathbf{v}), \quad (3)$$

where  $\mathbf{q} \in \mathcal{Q} \subseteq \mathbb{R}^{n_q}$ ,  $\mathbf{v} \in \mathcal{T}_q \mathcal{Q} \subseteq \mathbb{R}^{n_q}$ ,  $\mathbf{u} \in \mathbb{R}^{n_u}$ ,  $\boldsymbol{\lambda}_c \in \mathbb{R}^{n_c}$  and  $\mathbf{a}_c \in \mathbb{R}^{n_c}$  represent the configuration point, generalized velocity, control commands, contact forces, and contact acceleration, respectively. The functions  $\mathbf{M} : \mathcal{Q} \rightarrow \mathbb{R}^{n_q \times n_q}$  represent the joint-space inertia matrix,  $\boldsymbol{\tau} : \mathbb{R}^{n_u} \rightarrow \mathbb{R}^{n_q}$  denotes the joint-generalized torque,  $\mathbf{J}_c : \mathcal{Q} \rightarrow \mathbb{R}^{n_c \times n_q}$  is the contact Jacobian, and  $\mathbf{h} : \mathcal{Q} \times \mathcal{T}_q \mathcal{Q} \rightarrow \mathbb{R}^{n_q}$  is a force vector containing the Coriolis, centrifugal and gravitational terms. In the absence of contacts, free dynamics are governed by Eq. (2) with  $\boldsymbol{\lambda}_c = \mathbf{0}$ . We define unilateral conditions of Eq. (3) by penalizing negative contact forces [29]. Finally, this contact model neglects slippages and the presence of joint friction.

Free dynamics are efficiently computed using the articulated body algorithm (ABA) [26]. In contrast, contact dynamics are commonly computed using a Schur-complement approach based on the IMM [30]. Moreover, analytical derivatives of contact dynamics with respect to  $\mathbf{q}$ ,  $\mathbf{v}$  and  $\boldsymbol{\tau}$  are computed based on the algorithms described in [24], as explained in [7]. These algorithms for computing dynamics and their derivatives are essential for real-time applications.

### B. Inertial parameters of rigid bodies

The spatial inertia of a rigid body  $i$ , encapsulating the body’s mass-density field  $\rho : \mathbb{R}^3 \rightarrow \mathbb{R}_{\geq 0}$ , can be defined using a vector  $\boldsymbol{\pi}_i \in \mathbb{R}^{10}$ , whose elements are

$$\boldsymbol{\pi}_i = [m \ h_x \ h_y \ h_z \ I_{xx} \ I_{xy} \ I_{yy} \ I_{xz} \ I_{yz} \ I_{zz}]^\top, \quad (4)$$

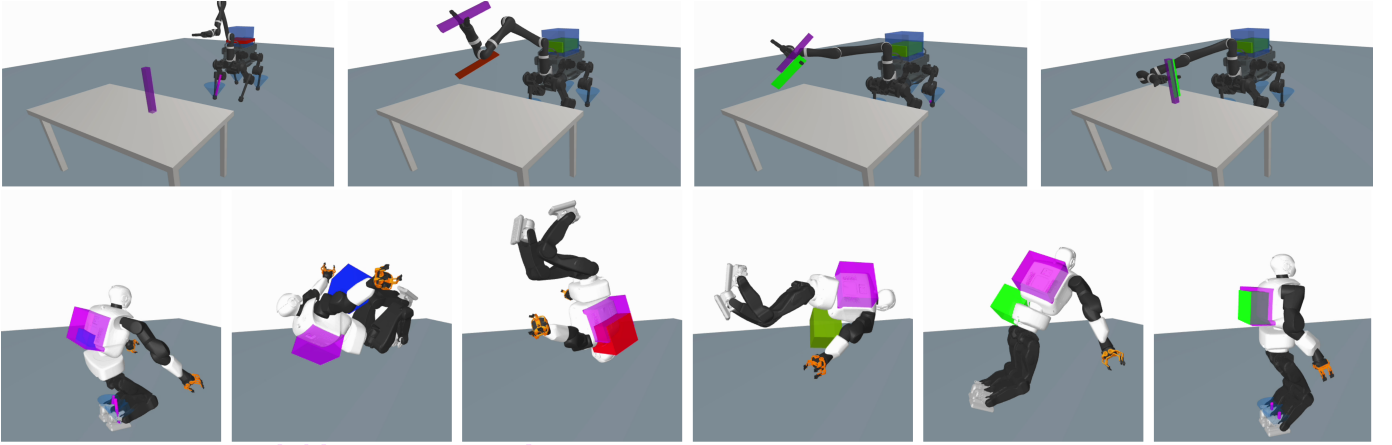


Fig. 2: Snapshots illustrating simulated online multi-contact inertial estimation and localization. (top) ANYmal with a Kinova arm carries an unknown payload while grasping an unknown object. (bottom) Talos performs a backflip while simultaneously estimating its backpack. Unknown payloads are represented in magenta, and upon convergence of the estimator, the estimated payload is depicted in green. The horizon of the estimator is set to the length of the simulation. To watch the video, click the picture or see [https://youtu.be/nDOxTgeK\\_5o](https://youtu.be/nDOxTgeK_5o).

where  $m \in \mathbb{R}$  denotes the body's mass,  $\mathbf{h} = [h_x \ h_y \ h_z]^\top = m\mathbf{c} \in \mathbb{R}^3$  represents the first mass moment with  $\mathbf{c}$  as its barycenter, and  $[I_{xx} \ I_{xy} \ I_{yy} \ I_{xz} \ I_{yz} \ I_{zz}]^\top$  are the elements of its inertia matrix  $\mathbf{I} \in \mathbb{R}^{3 \times 3}$ . Both barycenter and rotational inertia are expressed in the body-fixed reference frame as introduced in [23]. Moreover, the rotational inertia  $\mathbf{I}$  can be expressed at the barycenter using the parallel axis theorem:

$$\mathbf{I}_c = \mathbf{I} - \frac{\mathbf{S}(\mathbf{h})\mathbf{S}(\mathbf{h})^\top}{m}, \quad (5)$$

where  $\mathbf{S} : \mathbb{R}^3 \rightarrow \mathfrak{so}(3)$  is the skew-symmetric matrix, also known as the Lie algebra of  $SO(3)$  (see [8]).

As described in [23], the generalized torques can be expressed as an affine function of the inertial parameters  $\boldsymbol{\pi}$ , i.e.,

$$\boldsymbol{\tau}(\mathbf{u}) = \mathbf{Y}(\mathbf{q}, \mathbf{v}, \dot{\mathbf{v}})\boldsymbol{\pi}, \quad (6)$$

where  $\mathbf{Y} : \mathcal{Q} \times \mathcal{T}_q \mathcal{Q} \times \mathcal{T}_q \mathcal{Q} \rightarrow \mathbb{R}^{n_q \times 10n_b}$  is the joint-torque regressor matrix with  $n_b$  as the number of rigid bodies.

### C. Physically-consistent spatial inertia

We say that  $\boldsymbol{\pi}_i$  is *fully physically consistent*, or  $\boldsymbol{\pi}_i \in \mathcal{I}$ , if there exists a finite-value density function  $\rho$ . The set  $\mathcal{I} \subset \mathbb{R}^{10}$  is characterized by the following inequality constraints:

$$\begin{aligned} m > 0, \quad \mathbf{I}_c \succeq 0, \\ D_x < D_y + D_z, \quad D_y < D_x + D_z, \quad D_z < D_x + D_y. \end{aligned} \quad (7)$$

Here,  $\mathbf{D} = \text{diag}(D_x, D_y, D_z) \in \mathbb{R}^{3 \times 3}$  represents the principal moments of inertia, computed as  $\mathbf{I}_c = \mathbf{R}\mathbf{D}\mathbf{R}^\top$  with  $\mathbf{R} \in SO(3)$ . The condition  $\mathbf{I}_c \succeq 0$  ensures positivity in the principal components of inertia, and the triangle inequalities enforce positivity in second moments of mass [27].

The rotational inertia  $\mathbf{I}_c$  can be interpreted as a point-mass distribution with covariance  $\boldsymbol{\Sigma}_c$ . When mapping this to its spatial inertia, it results in a 4x4 pseudo-inertia matrix [31]:

$$\mathbf{J} = \begin{bmatrix} \boldsymbol{\Sigma} & \mathbf{h} \\ \mathbf{h}^\top & m \end{bmatrix}, \quad \text{where} \quad \boldsymbol{\Sigma} = \frac{1}{2}\text{Tr}(\mathbf{I})\mathbf{1}_3 - \mathbf{I}, \quad (8)$$

$\boldsymbol{\Sigma} = \boldsymbol{\Sigma}_c + m\mathbf{c}\mathbf{c}^\top$ ,  $\text{Tr}(\cdot)$  is the trace operator, and  $\mathbf{1}_3$  is a 3x3 identity matrix. The pseudo-inertia matrix  $\mathbf{J} \in \mathcal{S}_{++}^4$  must satisfy the condition  $\mathbf{J} \succeq 0$  for full physical consistency.

## III. PARAMETRIZATION OF INERTIAL PARAMETERS

To map parameters  $\boldsymbol{\theta}_i \in \mathbb{R}^{10}$  to fully physically consistent parameters  $\boldsymbol{\pi}_i \in \mathcal{I}$ , we can construct a smooth isomorphic mapping  $\boldsymbol{\psi}_i : \mathbb{R}^{10} \rightarrow \mathcal{I}$ . Below, we present two isomorphic mappings. First, we introduce log-Cholesky parametrization and then proceed to develop our *exponential eigenvalue parametrization*.

### A. Log-Cholesky parametrization

Log-Cholesky decompositions are applicable to semidefinite matrices, enabling us to encode the condition  $\mathbf{J}_i \succeq 0$  for physical consistency of body  $i$ . As suggested in [28], a log-Cholesky parametrization of the pseudo inertia  $\mathbf{J} = \mathbf{U}\mathbf{U}^\top$ , with

$$\mathbf{U} = e^\alpha \begin{bmatrix} e^{d_1} & s_{12} & s_{13} & t_1 \\ 0 & e^{d_2} & s_{23} & t_2 \\ 0 & 0 & s_{23} & t_3 \\ 0 & 0 & 0 & 1 \end{bmatrix}, \quad (9)$$

can be employed to establish an isomorphic map  $\boldsymbol{\pi} = \boldsymbol{\psi}(\boldsymbol{\theta}_{\text{chol}})$ . Here,  $\boldsymbol{\psi} := \text{vech}(\mathbf{U}\mathbf{U}^\top)$ , where the  $\text{vech}(\cdot)$  operator denotes the serialization operation of  $\mathbf{J}$ , and

$$\boldsymbol{\theta}_{\text{chol}} = [\alpha \ d_1 \ d_2 \ d_3 \ s_{12} \ s_{23} \ s_{13} \ t_1 \ t_2 \ t_3]^\top \in \mathbb{R}^{10}. \quad (10)$$

### B. Exponential eigenvalue parametrization

The singular value decomposition of  $\mathbf{I}_c$  can be expressed in terms of its second moments of mass:

$$\mathbf{I}_c = \mathbf{R} \overbrace{\text{diag}(\mathbf{P}\mathbf{L})}^{\mathbf{D}} \mathbf{R}^\top, \quad \text{where} \quad \mathbf{P} = \begin{bmatrix} 0 & 1 & 1 \\ 1 & 0 & 1 \\ 1 & 1 & 0 \end{bmatrix} \quad (11)$$

and  $\mathbf{L} = [L_x \ L_y \ L_z] \in \mathbb{R}_{\geq 0}^3$  denotes the second moments of mass. Ensuring positivity in  $L_x, L_y, L_z$  is equivalent to satisfying both  $\mathbf{I}_c \succeq 0$  and the triangle inequalities in Eq. (7). Intuitively, these conditions on  $L_x, L_y, L_z$ , and  $m \geq 0$  can be embedded using an exponential map. Formally, their manifold constraints are

$$\text{diag}(\mathbf{L}) \cdot \text{diag}(\mathbf{L})^{-1} = \mathbf{1}_3, \quad m \cdot m^{-1} = 1, \quad (12)$$

defining the real numbers as their Lie algebra structure. Therefore, our parametrization is given by

$$m = \exp(\sigma_m), \quad \mathbf{L} = [\exp(\sigma_x) \exp(\sigma_y) \exp(\sigma_z)]^\top, \quad (13)$$

where  $\sigma_m$  and  $(\sigma_x, \sigma_y, \sigma_z)$  denote the mass and rotational inertia parameters, respectively. Moreover, the structure of the rotational matrix  $\mathbf{R}$  is guaranteed by parametrizing it via the Lie algebra of  $SO(3)$ , i.e.,

$$\mathbf{R} = \text{Exp}(\boldsymbol{\omega}), \quad (14)$$

where  $\boldsymbol{\omega} = [\omega_x \ \omega_y \ \omega_z] \in \mathbb{R}^3 \cong \mathfrak{so}(3)$ , and  $\text{Exp} : \mathbb{R}^3 \rightarrow SO(3)$  converts this vector elements to the elements of the  $SO(3)$  group. Moreover, we obtain the inertia  $\mathbf{I}$  via Eq. (5).

Combining the exponential maps and stacking them into a vector, we construct a novel map with local submersion  $\boldsymbol{\pi} = \boldsymbol{\psi}(\boldsymbol{\theta}_{\text{eval}})$ , where

$$\boldsymbol{\theta}_{\text{eval}} = [\sigma_m \ h_x \ h_y \ h_z \ \omega_x \ \omega_y \ \omega_z \ \sigma_x \ \sigma_y \ \sigma_z]^\top \in \mathbb{R}^{10}. \quad (15)$$

Finally, we can analytically compute  $\frac{\partial \boldsymbol{\pi}}{\partial \boldsymbol{\theta}}$  for both  $\boldsymbol{\theta}_{\text{Ichol}}$  and  $\boldsymbol{\theta}_{\text{eval}}$ , as they are smooth and differentiable parametrizations.

#### IV. MULTI-CONTACT OPTIMAL ESTIMATION

Optimal estimation with hybrid events involves the use of multiphase dynamics and reset maps:

$$\min_{\mathbf{x}_s, \mathbf{w}_s, \boldsymbol{\theta}} \ell_N(\mathbf{x}_N; \boldsymbol{\theta} | \hat{\mathbf{z}}_N) + \sum_{k=0}^{N-1} \ell_k(\mathbf{x}_k, \mathbf{w}_k; \boldsymbol{\theta} | \hat{\mathbf{z}}_k) \quad (16)$$

s.t. for  $p \in \mathcal{P}$ :

for  $k \in \{p_0, p_0 + 1, \dots, p_N - 1\}$ :

$$\mathbf{x}_{k+1} = \mathbf{f}_p(\mathbf{x}_k; \boldsymbol{\theta} | \hat{\mathbf{u}}_k) \oplus \mathbf{w}_k \quad (\text{phase dyn.})$$

$$\mathbf{x}_{p_{N+1}} = \boldsymbol{\Delta}_p(\mathbf{x}_{p_N}; \boldsymbol{\theta}), \quad (\text{reset map})$$

where  $\mathbf{f}_p : \mathcal{X} \times \mathbb{R}^{n_\theta} \rightarrow \mathcal{T}_x \mathcal{X}$  describes the free or contact dynamics in phase  $p$ ,  $\boldsymbol{\Delta}_p : \mathcal{X} \times \mathbb{R}^{n_\theta} \rightarrow \mathcal{T}_x \mathcal{X}$  defines its contact-gain transition (modeled via impulse dynamics), and  $\ell_k$  encodes the observations  $\hat{\mathbf{z}}_k$  at the  $k$ -th node. Below, we describe our novel analytical derivatives w.r.t.  $\boldsymbol{\theta}$ , which is inspired from the analytical derivatives w.r.t.  $(\mathbf{q}, \mathbf{v})$  described in [7], [29].

##### A. Analytical derivatives of parametrized dynamics

In free dynamics, inertial parameters  $\boldsymbol{\pi} = (\pi_i)_{i=0}^{n_b}$  (with  $n_b$  denoting the number of bodies) exhibit a linear relationship with the generalized torques and  $\partial \text{FD} = \mathbf{M}^{-1} \partial \text{ID}$  holds, as the forward dynamics (FD) is the reciprocal of inverse dynamics (ID) [24]. Therefore, by applying the chain rule, we compute the analytical derivatives of forward dynamics with respect to  $\boldsymbol{\theta}$  as

$$\frac{\partial \text{FD}}{\partial \boldsymbol{\theta}} = \mathbf{M}(\mathbf{q})^{-1} \frac{\partial \text{ID}}{\partial \boldsymbol{\pi}} \frac{\partial \boldsymbol{\pi}}{\partial \boldsymbol{\theta}} = \mathbf{M}(\mathbf{q})^{-1} \mathbf{Y}(\mathbf{q}, \mathbf{v}, \dot{\mathbf{v}}) \frac{\partial \boldsymbol{\pi}}{\partial \boldsymbol{\theta}}. \quad (17)$$

Moving on to contact/phase dynamics  $\mathbf{f}_p$  of Section II-A, we apply the chain rule to derive the analytical derivatives for both the system's acceleration and the contact forces:

$$\frac{\partial}{\partial \boldsymbol{\theta}} \begin{bmatrix} \dot{\mathbf{v}} \\ -\boldsymbol{\lambda}_c \end{bmatrix} = - \begin{bmatrix} \mathbf{M}(\mathbf{q}) & \mathbf{J}_c(\mathbf{q})^\top \\ \mathbf{J}_c(\mathbf{q}) & \mathbf{0} \end{bmatrix}^{-1} \begin{bmatrix} \frac{\partial \boldsymbol{\tau}}{\partial \boldsymbol{\theta}} \\ \mathbf{0} \end{bmatrix}, \quad (18)$$

where  $\frac{\partial \boldsymbol{\tau}}{\partial \boldsymbol{\theta}} = \mathbf{Y}(\mathbf{q}, \mathbf{v}, \dot{\mathbf{v}}) \frac{\partial \boldsymbol{\pi}}{\partial \boldsymbol{\theta}}$  and  $\frac{\partial \boldsymbol{\pi}}{\partial \boldsymbol{\theta}}$  is the partial derivatives of the parametrization (see Section III). To enhance efficiency, this matrix inversion is performed via its Schur complement. This complement requires computing  $\mathbf{M}^{-1}$ . Similar to free dynamics, we achieve this through the Cholesky decomposition of  $\mathbf{M}$ , an approach typically employed in IMMs.

Similarly, derivatives of impulse/reset dynamics  $\boldsymbol{\Delta}_p$  involves inverting the same matrix but with:

$$\begin{aligned} \frac{\partial \boldsymbol{\tau}}{\partial \boldsymbol{\theta}} &:= \left( \frac{\partial \text{ID}(\mathbf{q}, \mathbf{0}, \mathbf{v}^+ - \mathbf{v})}{\partial \boldsymbol{\pi}} - \frac{\partial \text{ID}(\mathbf{q}, \mathbf{0}, \mathbf{0})}{\partial \boldsymbol{\pi}} \right) \frac{\partial \boldsymbol{\pi}}{\partial \boldsymbol{\theta}}, \\ &= (\mathbf{Y}(\mathbf{q}, \mathbf{0}, \mathbf{v}^+ - \mathbf{v}) - \mathbf{Y}(\mathbf{q}, \mathbf{0}, \mathbf{0})) \frac{\partial \boldsymbol{\pi}}{\partial \boldsymbol{\theta}}, \end{aligned} \quad (19)$$

where  $\mathbf{v}^+ \in \mathcal{T}_q \mathcal{Q} \subseteq \mathbb{R}^{n_q}$  is the post impact velocity.

#### V. DDP WITH PARAMETRIZED DYNAMICS

Handling parametrized dynamics requires to introduce an additional decision variable  $\boldsymbol{\theta}$ . To exploit its *temporal structure*, we begin by examining the optimality conditions through the lens of Bellman, ultimately leading to a parametrized Riccati recursion. For readers not familiar with numerical optimization, we provide a accompanying report in [32].

##### A. Optimality conditions

By examining the Bellman equation of Eq. (16), specifically,

$$\begin{aligned} \mathcal{V}(\mathbf{x}; \boldsymbol{\theta} | \hat{\mathbf{u}}, \hat{\mathbf{z}}) &= \min_{\mathbf{x}', \mathbf{x}, \mathbf{w}; \boldsymbol{\theta}} \ell(\mathbf{x}, \mathbf{w}; \boldsymbol{\theta} | \hat{\mathbf{z}}) + \mathcal{V}'(\mathbf{x}'; \boldsymbol{\theta} | \hat{\mathbf{u}}, \hat{\mathbf{z}}) \\ \text{s.t. } \mathbf{x}' &= \mathbf{f}(\mathbf{x}, \mathbf{w}; \boldsymbol{\theta} | \hat{\mathbf{u}}), \end{aligned} \quad (20)$$

we break the optimal estimation problem into a sequence of subproblems. The KKT point for each subproblem can be efficiently determined using the Newton method (i.e.,  $\nabla \mathbf{r} = -\mathbf{r}$ ), yielding the following linear system of equations:

$$\begin{array}{c} \overbrace{\begin{bmatrix} \mathcal{L}_{xx} & \mathcal{L}_{xw} & \mathcal{L}_{x\theta} & \mathbf{f}_x^\top \\ \mathcal{L}_{xw}^\top & \mathcal{L}_{ww} & \mathcal{L}_{w\theta} & \mathbf{f}_w^\top \\ \mathcal{L}_{x\theta}^\top & \mathcal{L}_{w\theta}^\top & \mathcal{L}_{\theta\theta} & \mathbf{f}_\theta^\top \\ \mathbf{f}_x & \mathbf{f}_w & \mathbf{f}_\theta & -\mathbf{I} \end{bmatrix}}^{\nabla \mathbf{r}} \quad \overbrace{\begin{bmatrix} \delta \mathbf{x} \\ \delta \mathbf{w} \\ \delta \boldsymbol{\theta} \\ \boldsymbol{\xi}^+ \\ \delta \mathbf{x}' \end{bmatrix}}^{\delta \mathbf{r}} = - \overbrace{\begin{bmatrix} \ell_x \\ \ell_w \\ \ell_\theta + \mathcal{V}'_\theta \\ \bar{\mathbf{f}} \\ \mathcal{V}'_x \end{bmatrix}}^{\mathbf{r}} \end{array} \quad (21)$$

with:

$$\begin{aligned} \boldsymbol{\xi}^+ &:= \boldsymbol{\xi} + \delta \boldsymbol{\xi}, & \bar{\mathbf{f}} &:= \mathbf{f}(\mathbf{x}, \mathbf{w}; \boldsymbol{\theta}) \ominus \mathbf{x}', \\ \mathcal{L}_{xx} &:= \ell_{xx} + \mathcal{V}'_x \cdot \mathbf{f}_{xx}, & \mathcal{L}_{xw} &:= \ell_{xw} + \mathcal{V}'_x \cdot \mathbf{f}_{xw}, \\ \mathcal{L}_{x\theta} &:= \ell_{x\theta} + \mathcal{V}'_x \cdot \mathbf{f}_{x\theta}, & \mathcal{L}_{ww} &:= \ell_{ww} + \mathcal{V}'_x \cdot \mathbf{f}_{ww}, \\ \mathcal{L}_{w\theta} &:= \ell_{w\theta} + \mathcal{V}'_x \cdot \mathbf{f}_{w\theta}, & \mathcal{L}_{\theta\theta} &:= \ell_{\theta\theta} + \mathcal{V}'_{\theta\theta} + \mathcal{V}'_x \cdot \mathbf{f}_{\theta\theta}, \end{aligned}$$

where  $\mathbf{r}$  represents the residual vector containing the gradient of the Lagrangian of Eq. (20). In Eq. (21),  $\ell_p$ ,  $\mathbf{f}_p$ , are the first derivative of the cost and the system dynamics with respect to  $\mathbf{p}$ , with  $\mathbf{p}$  a hypothetical decision variable that represents  $\mathbf{x}$ ,  $\mathbf{w}$  or  $\boldsymbol{\theta}$ ;  $\ell_{pp}$ ,  $\mathbf{f}_{pp}$  are the second derivatives;  $\mathcal{V}'_p$ ,  $\mathcal{V}'_{pp}$  are the gradient and Hessian of the value function;  $\bar{\mathbf{f}}$  describe the infeasibility in the dynamics;  $\boldsymbol{\xi}$  is the Lagrange multiplier associated to the dynamics;  $\delta \mathbf{x}$ ,  $\delta \mathbf{w}$ ,  $\delta \boldsymbol{\theta}$ ,  $\delta \mathbf{x}'$  and  $\delta \boldsymbol{\xi}$  provides the search direction computed for the primal and dual variables, respectively; and the *prime* superscript is used to refer to the next node.

Similar to optimal control [14, Section 2.2], by inspecting the last row of Eq. (21) we observe the presence of the Markovian structure, leading to  $\xi^+ = \mathcal{V}'_x + [\mathcal{V}'_{xx} \quad \mathcal{V}'_{x\theta}] \begin{bmatrix} \delta x \\ \delta \theta \end{bmatrix}$ . This connection becomes evident when augmenting the system's state with its parameters  $\theta$ , contributing to the condensation of the system of equations in Eq. (21) as:

$$\begin{bmatrix} \mathbf{Q}_{xx} & \mathbf{Q}_{xw} & \mathbf{Q}_{x\theta} \\ \mathbf{Q}_{xw}^\top & \mathbf{Q}_{ww} & \mathbf{Q}_{w\theta} \\ \mathbf{Q}_{x\theta}^\top & \mathbf{Q}_{w\theta}^\top & \mathbf{Q}_{\theta\theta} \end{bmatrix} \begin{bmatrix} \delta x \\ \delta w \\ \delta \theta \end{bmatrix} = - \begin{bmatrix} \mathbf{Q}_x \\ \mathbf{Q}_w \\ \mathbf{Q}_\theta \end{bmatrix}, \quad (22)$$

where the  $\mathbf{Q}$ 's terms represent the local approximation of the *action-value function* whose expressions are:

$$\begin{aligned} \mathbf{Q}_{xx} &= \mathcal{L}_{xx} + \mathbf{f}_x^\top \mathcal{V}'_{xx} \mathbf{f}_x, & \mathbf{Q}_{w\theta} &= \mathcal{L}_{w\theta} + \mathbf{f}_w^\top (\mathcal{V}'_{x\theta} + \mathcal{V}'_{xx} \mathbf{f}_\theta), \\ \mathbf{Q}_{xw} &= \mathcal{L}_{xw} + \mathbf{f}_x^\top \mathcal{V}'_{xx} \mathbf{f}_w, & \mathbf{Q}_{x\theta} &= \mathcal{L}_{x\theta} + \mathbf{f}_x^\top (\mathcal{V}'_{x\theta} + \mathcal{V}'_{xx} \mathbf{f}_\theta), \\ \mathbf{Q}_{ww} &= \mathcal{L}_{ww} + \mathbf{f}_w^\top \mathcal{V}'_{xx} \mathbf{f}_w, & \mathbf{Q}_{\theta\theta} &= \mathcal{L}_{\theta\theta} + \mathbf{f}_\theta^\top (2\mathcal{V}'_{x\theta} + \mathcal{V}'_{xx} \mathbf{f}_\theta), \\ \mathbf{Q}_x &= \ell_x + \mathbf{f}_x^\top \mathcal{V}_x^+, & \mathbf{Q}_\theta &= \ell_\theta + \mathcal{V}_\theta^+ + \mathbf{f}_\theta^\top \mathcal{V}_x^+, \\ \mathbf{Q}_w &= \ell_w + \mathbf{f}_w^\top \mathcal{V}_x^+ \end{aligned} \quad (23)$$

with  $\mathcal{V}_x^+ := \mathcal{V}'_x + \mathcal{V}'_{xx} \bar{\mathbf{f}}$  and  $\mathcal{V}_\theta^+ := \mathcal{V}'_\theta + \mathcal{V}'_{x\theta} \bar{\mathbf{f}}$  as the gradients of the value function after the deflection produced by the dynamics infeasibility  $\bar{\mathbf{f}}$  (see [7]). To exploit the *parametric structure*, we then compute the estimation policy and value function as functions of the parameters and arrival state.

### B. Policy and value function

Eq. (22) computes the KKT point of a quadratic program that locally minimizes the Bellman equation Eq. (20), i.e.,

$$\delta \mathcal{V}(\delta x; \delta \theta | \hat{\mathbf{u}}, \hat{\mathbf{z}}) \simeq \min_{\delta w} \frac{1}{2} \begin{bmatrix} 1 \\ \delta x \\ \delta w \\ \delta \theta \end{bmatrix}^\top \begin{bmatrix} \mathbf{Q}_x & \mathbf{Q}_{xx} & \mathbf{Q}_{xw} & \mathbf{Q}_{x\theta} \\ \mathbf{Q}_w & \mathbf{Q}_{xw}^\top & \mathbf{Q}_{ww} & \mathbf{Q}_{w\theta} \\ \mathbf{Q}_\theta & \mathbf{Q}_{x\theta}^\top & \mathbf{Q}_{w\theta}^\top & \mathbf{Q}_{\theta\theta} \end{bmatrix} \begin{bmatrix} 1 \\ \delta x \\ \delta w \\ \delta \theta \end{bmatrix}. \quad (24)$$

Moreover, we compute  $\delta w$  as a function of  $\delta x$  and  $\delta \theta$  from Eq. (22). This leads to what we call the *DDP approach* for optimal estimation, as it computes an *estimation policy*  $\delta w$  given observations  $(\hat{\mathbf{u}}, \hat{\mathbf{z}})$ , i.e.,

$$\delta w = -\mathbf{k} - \mathbf{K} \delta x - \mathbf{P} \delta \theta, \quad (25)$$

where  $\mathbf{k} = \mathbf{Q}_{ww}^{-1} \mathbf{Q}_w$ ,  $\mathbf{K} = \mathbf{Q}_{ww}^{-1} \mathbf{Q}_{xw}^\top$  and  $\mathbf{P} = \mathbf{Q}_{ww}^{-1} \mathbf{Q}_{w\theta}$  are the feed-forward and feedback terms. In this approach, when plugging the changes in the estimation into Eq. (24), we obtain a quadratic approximation of the *optimal arrival cost* (a.k.a. value function) as follows

$$\begin{aligned} \delta \mathcal{V}(\delta x; \delta \theta | \hat{\mathbf{u}}, \hat{\mathbf{z}}) &\simeq \Delta \mathcal{V}_1 + \frac{\Delta \mathcal{V}_2}{2} \\ &+ \frac{1}{2} \begin{bmatrix} \delta x \\ \delta \theta \end{bmatrix}^\top \begin{bmatrix} \mathcal{V}_{xx} & \mathcal{V}_{x\theta} \\ \mathcal{V}_{x\theta}^\top & \mathcal{V}_{\theta\theta} \end{bmatrix} \begin{bmatrix} \delta x \\ \delta \theta \end{bmatrix} + \begin{bmatrix} \mathcal{V}_x \\ \mathcal{V}_\theta \end{bmatrix}^\top \begin{bmatrix} \delta x \\ \delta \theta \end{bmatrix}, \end{aligned} \quad (26)$$

where

$$\begin{aligned} \Delta \mathcal{V}_1 &= -\mathbf{k}^\top \mathbf{Q}_w, & \Delta \mathcal{V}_2 &= \mathbf{k}^\top \mathbf{Q}_{ww} \mathbf{k}, \\ \mathcal{V}_x &= \mathbf{Q}_x - \mathbf{Q}_{xw} \mathbf{k}, & \mathcal{V}_\theta &= \mathbf{Q}_\theta - \mathbf{Q}_{w\theta}^\top \mathbf{k}, \\ \mathcal{V}_{xx} &= \mathbf{Q}_{xx} - \mathbf{Q}_{xw} \mathbf{K}, & \mathcal{V}_{\theta\theta} &= \mathbf{Q}_{\theta\theta} - \mathbf{Q}_{w\theta}^\top \mathbf{P}, \\ \mathcal{V}_{x\theta} &= \mathbf{Q}_{x\theta} - \mathbf{Q}_{xw} \mathbf{P}, \end{aligned} \quad (27)$$

and  $\mathbf{Q}_{xw} \mathbf{P} = \mathbf{K}^\top \mathbf{Q}_{w\theta}$ .

To compute the search directions  $\delta \theta$ , we analyze the conditions of optimality for the initial node detailed below. Unlike the approach in [19], our method calculates  $\delta \theta$  while simultaneously estimating the unknown arrival state  $\delta x_0$  and accounting for dynamics infeasibilities.

### C. Arrival state and parameters

By substituting Eq. (25) into the condensed KKT equations of the arrival node in Eq. (22), we obtain:

$$\begin{bmatrix} \mathcal{V}_{xx}^\bullet & \mathcal{V}_{x\theta}^\bullet \\ \mathcal{V}_{x\theta}^{\bullet\top} & \mathcal{V}_{\theta\theta}^\bullet \end{bmatrix} \begin{bmatrix} \delta x_0 \\ \delta \theta \end{bmatrix} = - \begin{bmatrix} \mathcal{V}_x^\bullet \\ \mathcal{V}_\theta^\bullet \end{bmatrix}, \quad (28)$$

where the *bullet* superscript is used to refer to the arrival node (e.g.,  $\delta x_0 := \delta x^\bullet$ ). Next, we describe two methods for factorizing Eq. (28) namely the Schur-complement and nullspace methods.

1) *Schur-complement method*: It computes both  $\delta \theta$  and  $\delta x_0$  by factorizing Eq. (28) via the Schur-complement approach. This results in the following expressions:

$$\delta \theta = -\mathbf{k}_\theta - \mathbf{K}_\theta \delta x_0, \quad \delta x_0 := -\mathcal{V}_{xx_0}^{-1} \mathcal{V}_{x_0}, \quad (29)$$

where  $\mathbf{k}_\theta = \mathcal{V}_{\theta\theta}^{\bullet-1} \mathcal{V}_\theta^\bullet$ ,  $\mathbf{K}_\theta = \mathcal{V}_{\theta\theta}^{\bullet-1} \mathcal{V}_{x\theta}^{\bullet\top}$  are the feed-forward and feedback terms of the parameters update  $\delta \theta$ ,

$$\mathcal{V}_{x_0} = \mathcal{V}_x^\bullet - \mathcal{V}_{x\theta}^\bullet \mathbf{k}_\theta, \quad \mathcal{V}_{xx_0} = \mathcal{V}_{xx}^\bullet - \mathcal{V}_{x\theta}^\bullet \mathbf{K}_\theta, \quad (30)$$

are the derivatives of the value function associated to arrival node after updating the system's parameters, and  $\mathcal{V}_{xx_0}$  is of the Schur complement of Eq. (28). Now, we can rewrite the changes of the estimation policy as  $\delta w = -\bar{\mathbf{k}} - \mathbf{K} \delta x$ , where  $\bar{\mathbf{k}} = \mathbf{k} + \mathbf{P} \delta \theta$  represents the entire feed-forward term.

2) *Nullspace method*: It parametrizes the search direction for the parameters as  $\delta \theta = \mathbf{Y} \delta \theta_y + \mathbf{Z} \delta \theta_z$ . Here,  $\mathbf{Z} \in \mathbb{R}^{n_\theta \times n_z}$  is the nullspace basis of  $\mathcal{V}_{\theta\theta}^\bullet$  and  $\mathbf{Y} \in \mathbb{R}^{n_\theta \times n_y}$  is its orthogonal matrix. Then, by substituting this parametrization into the second term of Eq. (29) and observing that  $\mathcal{V}_{\theta\theta}^\bullet \mathbf{Z} = \mathbf{0}$ , we obtain

$$\mathbf{Y}^\top \mathcal{V}_{\theta\theta}^\bullet \mathbf{Y} \delta \theta_y = - \overbrace{\mathbf{Y}^\top \mathcal{V}_\theta^\bullet}^{\mathbf{k}_{\theta y}} - \overbrace{\mathbf{Y}^\top \mathcal{V}_{x\theta}^{\bullet\top}}^{\mathbf{K}_{\theta y}} \delta x_0, \quad (31)$$

where we pre-multiply by  $\mathbf{Y}^\top$  to ensure the squareness of  $\mathcal{V}_{\theta\theta}^\bullet \mathbf{Y}$ . Eq. (31) is then solved efficiently using a Cholesky decomposition as  $\mathbf{Y}^\top \mathcal{V}_{\theta\theta}^\bullet \mathbf{Y}$  is a positive definite symmetric matrix. Finally, we recover the search direction for the parameters as  $\delta \theta = \mathbf{Y} \delta \theta_y$  and  $\delta x_0$  from the second term of Eq. (29).

The asymptotic computational complexity of our Riccati recursion is  $\mathcal{O}(\mathcal{N}(n_x + n_x)^3 + n_\theta^3)$  flops,<sup>1</sup> which shows potential for real-time applications. This is because full-dynamics MPC algorithms with similar complexity have demonstrated the capability to run at high frequencies (e.g., [29]).

<sup>1</sup>For more details on algorithmic complexity of Riccati recursion, we refer to [33].



#### D. Forward rollouts and merit function

The search directions obtained from Eqs. (25), (29) and (31) provide updates for the system’s uncertainties, parameters, and arrival state. To determine the step length along these directions, we perform a forward rollout of the disturbed system’s dynamics and evaluate the associated costs. Below, we describe our novel approach inspired by optimal control literature, known as multiple shooting. Let’s start by describing how we update the arrival state and parameters first.

1) *Arrival state and parameters update:* We follow a line-search approach to update the arrival state and system’s parameters, i.e.,

$$\mathbf{x}_0^+ = \mathbf{x}_0 \oplus \alpha \delta \mathbf{x}_0, \quad \boldsymbol{\theta}^+ = \boldsymbol{\theta} + \alpha \delta \boldsymbol{\theta}, \quad (32)$$

where  $\alpha \in (0, 1]$  denotes the step length and the *plus* superscript is used to denote the next guess under evaluation.

2) *Multiple shooting rollout:* Building upon classical line-search procedures in optimal control (see [34, Chapter 3]), our multiple shooting approach tries a linear rollout and updates the gaps based on nonlinear shoots, i.e.,

$$\begin{aligned} \mathbf{w}_k^+ &= \mathbf{w}_k + \alpha \delta \mathbf{w}_k, \\ \mathbf{x}_{k+1}^+ &= \mathbf{x}_{k+1} \oplus \alpha \delta \mathbf{x}_{k+1}, \\ \bar{\mathbf{f}}_{k+1}^+ &= \mathbf{f}(\mathbf{x}_k^+, \mathbf{w}_k^+; \boldsymbol{\theta}_k^+) \ominus \mathbf{x}_{k+1}^+, \end{aligned} \quad (33)$$

for  $k \in \{0, \dots, N\} \subset \mathbb{N}$ . Compared to the feasibility-driven rollout in [7], multiple shooting rollouts can be broken into two parallel loops: one for the update of the uncertainties  $\mathbf{w}_k^+$  and state  $\mathbf{x}_{k+1}^+$ , and another one for the update of the dynamics infeasibilities  $\bar{\mathbf{f}}_{k+1}^+$  and costs  $\ell_k(\mathbf{x}_k^+, \mathbf{w}_k^+)$ . Below, we describe how we evaluate the goodness of a given step length  $\alpha$ .

3) *Merit function:* We develop a merit function inspired by [21]. Specifically, it computes the expected cost reduction as a local approximation of the value function while being aware of the dynamics infeasibilities. More details can be found in our technical report [32]. Finally, we utilize (1) a nonmonotone step acceptance strategy based on Armijo conditions and (2) a Levenberg-Marquardt scheme as in [21].

## VI. RESULTS

We evaluate our multi-contact inertial parameters estimation and localization framework as follows. First, we compare the numerical performance of our exponential eigenvalue parametrization in Eq. (13) against the log-Cholesky in Eq. (10) approach. Second, we analyze the effect of multiple shooting approaches in optimal estimation. Third, we experimentally validate the advantages of updating inertial parameters for carrying unknown payloads. Finally, we show the importance of using hybrid dynamics for localization in agile maneuvers. We refer the reader to the video, where the benefits of our nullspace resolution are showcased.

#### A. Log-Cholesky vs Exponential Eigenvalue

This numerical analysis encompasses four diverse robotics systems: the Kinova arm, the Hector quadrotor, the ANYmal quadruped, and the Talos biped. In each scenario, we generated

dynamically-consistent trajectories by integrating observations from simulated joint encoders ( $\hat{\mathbf{q}}_j, \hat{\mathbf{v}}_j$ ), torso’s IMU data (linear acceleration  $\hat{\mathbf{q}}_i$ , gyroscopic velocities  $\hat{\boldsymbol{\omega}}_i$ , and orientations), and joint efforts  $\hat{\mathbf{u}}$ . To ensure a fair comparison between parameterizations, we omitted the parameter regularization term  $\|\boldsymbol{\theta} - \bar{\boldsymbol{\theta}}\|_{\Sigma_{\boldsymbol{\theta}}}^2$  from Eq. (1). Moreover, we initialized the inertial parameters for all the bodies with the same error of 70%. For the ANYmal and Talos robots, we included the contact constraints in Eq. (3). All the cases incorporated the multibody dynamics described in Eq. (2).

In each scenario illustrated in Fig. 3, both parametrizations converge to the same estimated trajectory, resulting in identical estimation errors (Fig. 3-bottom). Nevertheless, the exponential eigenvalue parametrization demonstrated superior performance, characterized by faster convergence rates and often lower cost values (Fig. 3-top). This can be attributed to its lower degree of nonlinearity compared to the log-Cholesky parametrization. Furthermore, the exponential eigenvalue parametrization offers a direct physical interpretation, which is particularly advantageous when partial knowledge of the rotational inertia is available. This is because it enables us to easily tune covariances in known inertial parameters  $\Sigma_{\boldsymbol{\theta}}$ , enhancing results in our trials with the Go1 robot.

#### B. Numerical effect of rollout strategies

To evaluate the numerical impact of our feasibility-driven [32, Eq. (30)] and multiple shooting rollouts in Eq. (33), we randomly generated 100 initial guesses and compared their convergence, cost and estimation errors against single shooting approaches (i.e., approach developed in [19]). In Table I, we observe that multiple shooting rollouts reduced the costs or estimation errors across all cases. Moreover, single shooting rollouts have a reduced basin of attraction to local minima and can encounter difficulties in convergence for challenging cases. Multiple shooting rollouts enabled us to handle the agile maneuvers in Fig. 2.

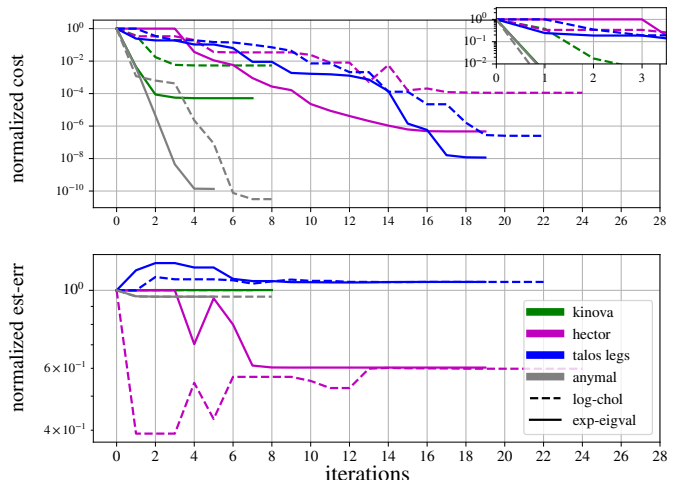


Fig. 3: Top: Local convergence for both parametrizations, showing better convergence the *exponential eigenvalue* (exp-eigval) parametrization in all cases. Bottom: Evolution of the estimation error, computed as the  $\ell_1$ -norm of difference between the optimized trajectory and the nominal one. Both parametrizations converge to the same local minima.

TABLE I: Rollout’s local convergence computed from 100 randomly initial guesses on three robotics systems.  $P$ -value obtained from an ANOVA analysis after applying Bonferroni correction.

		Iterations	Cost [ $\cdot 10^{-1}$ ]	Error [ $\ell_\infty$ -norm]
<i>Kinova</i>	single	39.7 $\pm$ 11.2	2.78 $\pm$ 0.89	3.11 $\pm$ 0.56
	feasible	<b>44.7 <math>\pm</math> 11.6</b>	1.16 $\pm$ 0.42	3.12 $\pm$ 0.01
	multiple	99.4 $\pm$ 71.5	<b>0.61 <math>\pm</math> 0.42</b>	<b>2.67 <math>\pm</math> 0.06</b>
	$p$ -value	$1.19 \cdot 10^{-60}$	$1.64 \cdot 10^{-17}$	$1.08 \cdot 10^{-5}$
<i>Quadrotor</i>	single	140.9 $\pm$ 65.1	0.12 $\pm$ 0.04	10.74 $\pm$ 0.0023
	feasible	150.1 $\pm$ 59.3	0.26 $\pm$ 0.11	10.74 $\pm$ 0.0013
	multiple	<b>16.9 <math>\pm</math> 19.1</b>	<b>0.07 <math>\pm</math> 1.31</b>	<b>10.74 <math>\pm</math> 0.0002</b>
	$p$ -value	$3.51 \cdot 10^{-5}$	$2.04 \cdot 10^{-85}$	$1.26 \cdot 10^{-22}$
<i>ANYmal</i>	single	×	×	×
	feasible	198.3 $\pm$ 16.6	0.22 $\pm$ 0.08	6.12 $\pm$ 0.92
	multiple	<b>14.1 <math>\pm</math> 14.8</b>	<b>0.01 <math>\pm</math> 1.65</b>	<b>6.02 <math>\pm</math> 0.22</b>
	$p$ -value	$2.07 \cdot 10^{-79}$	$5.64 \cdot 10^{-4}$	$7.41 \cdot 10^{-4}$

×algorithm does not find a solution within 200 iterations.

### C. Validation on the Go1 robot

We validated our multi-contact inertial estimation and localization in experimental trials with the Go1 robot. To showcase its capability in inertial parameters estimation, we added an unknown payload of 7.2 kg to the robot’s torso. The observations were recorded when the Go1’s predictive controller [29] was unaware of the additional payload (Fig. 4-top).

We integrated a variety of proprioceptive measurements  $\hat{\mathbf{z}} \in \mathcal{Z}$  in Eq. (1) with a step integration interval of 1 ms. First, we included joint positions  $\hat{\mathbf{q}}_j \in \mathbb{R}^{12}$  measured from encoders and numerically differentiated them to account for joint velocities  $\hat{\mathbf{v}}_j \in \mathbb{R}^{12}$ . Second, we derived Go1’s torso rotation from the IMU’s sensor fusion algorithm. This was incorporated with the following observation model  $\|\hat{\mathbf{R}}_b \ominus \mathbf{R}_b\|_{\Sigma_{\mathbf{R}}}^2$ . Here,  $\hat{\mathbf{R}}_b \ominus \mathbf{R}_b$  denotes the SO(3) inverse composition between the measured body orientation  $\hat{\mathbf{R}}_b$  and the estimated one  $\mathbf{R}_b$  and  $\Sigma_{\mathbf{R}} \in S(3)$  represents the covariance estimated by the sensor fusion algorithm. Third, we pre-integrated the IMU’s linear acceleration to obtain the torso’s linear velocities. This

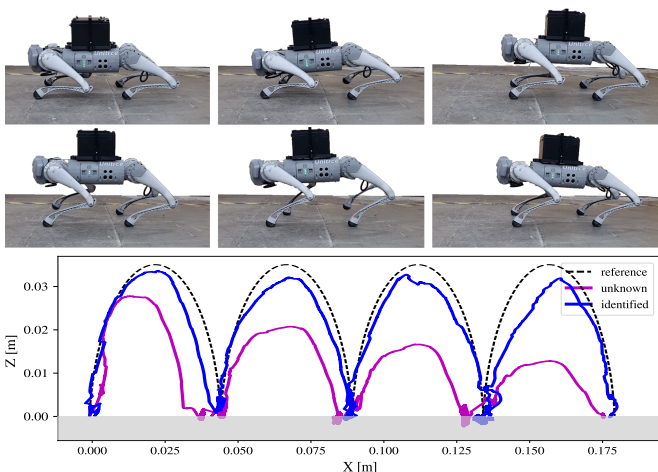


Fig. 4: Top: Go1 performing four walking gaits while carrying an unknown payload. In the top snapshots, Go1 struggled to maintain its posture due to model mismatch in the MPC. In the bottom snapshots, after correctly estimating the robot’s payload, Go1 confidently maintained its nominal posture. Bottom: Foot-swing tracking, the foot position is obtained from the VICON system, ignoring any localization effects. Our MPC encountered difficulties in tracking the reference swing-foot trajectory (dashed line) when the payload was unknown (magenta line). Specifically, the Go1 robot failed to reach the desired step height, an error accumulated over time. In contrast, our MPC improved its foot-swing tracking performance when our estimator identified the payload (blue line).

TABLE II: Identification errors of the unknown payload in the Go1 experimental trials. The window size for the Savitzky–Golay filter used in the least squares (LS) method is indicated in braces.

Gaussian noise $\sigma$	LS [100ms]	LS [10ms]	OE (ours)
0.0	102.20%	<b>3.87%</b>	<b>2.27%</b>
0.005	101.51%	<b>8.9%</b>	<b>2.28%</b>
0.01	102.06%	38.48%	<b>2.54%</b>
0.1	34.98%	170.48%	<b>4.67%</b>

observation also encompasses the IMU’s angular velocities, both of them are expressed in local coordinates for efficiency reasons. We estimated the contact sequence (see Fig. 5-top) using PRONTO’s default method, which is based on the contact forces estimated through a standard algorithm that utilizes the dynamic model in Eqs. (2) and (3). Lastly, we incorporated the torque commands  $\hat{\mathbf{u}} \in \mathbb{R}^{12}$  applied by the MPC controller.

1) *Estimating an unknown payload*: To showcase the importance of a correct estimation of the inertial parameters we ran our optimal estimator offline. Within the estimation horizon of 14s, it accurately determined the total payload, equivalent to a mass of 7.364 kg after 27 iterations. Subsequently, we updated the inertial parameters of Go1’s torso in its full-dynamics MPC controller. The impact of this update is vividly illustrated in Fig. 4-top. Concretely, it enabled the Go1 robot to maintain a stable posture during walking, emphasizing the significance of correcting model mismatches even for our fast MPC running at 50 Hz.

The payload estimation significantly influences the tracking capabilities of the swing foot, as depicted in Fig. 4-bottom. A comparison between swing trajectories with and without estimated inertial parameters reveals the crucial role it plays. In the absence of accurate inertial parameters, the MPC struggled to track reference swing trajectories, resulting in a progressively decaying motion. Instead, when the inertia was estimated, the MPC adeptly tracked the swing trajectory.

2) *Comparison of our optimal estimator with least squares*: To evaluate the performance of our inertial estimation method, we compared its accuracy with the regression (least squares) approach proposed in [28]. Table II presents the identification errors for both methods. For the least squares method, accelerations for the joint-torque regressor were computed via numerical differentiation and processed using a filtering technique. Results are provided for two filter configurations: a suggested 100 ms window in [28] and an improved 10 ms window. Each row in the table includes results for datasets with a possible Gaussian noise added to all observations.

The least squares method exhibits a high sensitivity to acceleration values, making the choice of filter a critical factor in the accuracy of inertial estimation. This sensitivity underscores the advantages of our Bayesian approach, which also handles localization uncertainties.

3) *Localization with hybrid dynamics*: To show the importance of a dynamic model in estimation, we compared our multi-contact localization approach against PRONTO [35]—a widely adopted localization framework for legged robots based on extended Kalman filter (EKF) and kinematics. PRONTO and our optimal estimator were configured to integrate the same proprioceptive information (namely IMU and encoders), contact estimation, integration step, and covariances. To provide a holistic evaluation, we employed PRONTO to close the loop with our MPC. Fig. 5-bottom shows localization errors for both estimators, measured with a motion capture system.

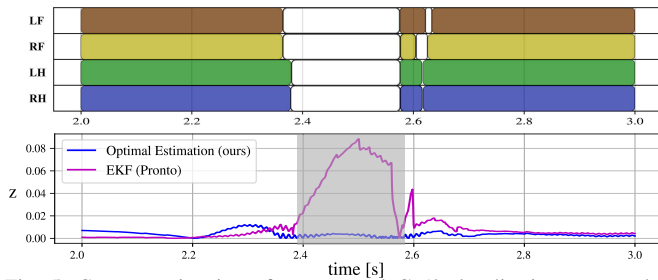


Fig. 5: Contact estimation of contact and Go1’s localization errors when performing a jump. Our optimal estimator (blue lines) exhibits a smaller estimation error compared to PRONTO.

The inclusion of hybrid dynamics significantly improved localization accuracy, especially in the presence of a dynamic maneuver like a jump, surpassing the estimation accuracy of PRONTO’s estimation. This achievement is possible because introducing dynamics effectively corrects nearly all IMU drifts, highlighting the critical role of relying on the robot’s dynamics to mitigate and correct this drift. We also anticipate similar performance compared to traditional factor graph methods when relying on kinematic models. This is because kinematic models struggle to accurately predict flying motions.

## VII. CONCLUSION

We introduced (i) a multiple shooting optimal estimation algorithm tailored for multi-contact inertial estimation and localization and (ii) a novel smooth manifold with local submersion, named exponential eigenvalue, to ensure the full physical consistency of inertial parameters. Our exponential eigenvalue manifold was compared against the singularity-free log-Cholesky manifold, demonstrating improved convergence attributed to its reduced degree of nonlinearity. However, it presented singularities with symmetrical inertias. To address this, we proposed a nullspace approach, which handles these rank deficiencies. Additionally, our multiple shooting rollout demonstrated superior numerical behavior compared to existing methods, resulting in better estimations. We demonstrated the effectiveness of our framework in complex scenarios such as humanoid brachiation and backflips, achieving higher accuracy than a conventional least squares approach. Practical benefits were further illustrated through experimental trials on the Go1 robot. Future work will involve an open-source C++ implementation.

## REFERENCES

- [1] J. Crassidis and J. Junkins, *Optimal Estimation of Dynamic Systems*. Chapman and Hall, 2004.
- [2] C. Forster, L. Carlone, F. Dellaert, and D. Scaramuzza, “On-Manifold Preintegration for Real-Time Visual-Inertial Odometry,” *IEEE Trans. Rob. (T-RO)*, vol. 33, 2017.
- [3] D. Wisth, M. Camurri, and M. Fallon, “VILENS: Visual, Inertial, Lidar, and Leg Odometry for All-Terrain Legged Robots,” *IEEE Rob. Autom. Lett. (RA-L)*, vol. 39, 2023.
- [4] P.-B. Wieber, “Holonomy and nonholonomy in the dynamics of articulated motion,” in *Fast Motions in Biomechanics and Robotics*, 2005.
- [5] R. Orsolino, M. Focchi, C. Mastalli, H. Dai, D. Caldwell, and C. Semini, “Application of Wrench-Based Feasibility Analysis to the Online Trajectory Optimization of Legged Robots,” *IEEE Rob. Autom. Lett. (RA-L)*, vol. 3, 2018.
- [6] D. Gabay, “Minimizing a differentiable function over a differential manifold,” *J. Optim. Theory Appl.*, vol. 37, 1982.

- [7] C. Mastalli, R. Budhiraja, W. Merkt, G. Saurel, B. Hammoud, M. Naveau, J. Carpentier, L. Righetti, S. Vijayakumar, and N. Mansard, “Crocodyl: An Efficient and Versatile Framework for Multi-Contact Optimal Control,” in *IEEE Int. Conf. Rob. Autom. (ICRA)*, 2020.
- [8] J. Sola, J. Deray, and D. Atchuthan, “A micro Lie theory for state estimation in robotics,” *arXiv preprint arXiv:1812.01537*, 2018.
- [9] J. T. Betts, *Practical Methods for Optimal Control and Estimation Using Nonlinear Programming*. Cambridge University Press, 2009.
- [10] P. E. Gill, W. Murray, and M. A. Saunders, “SNOPT: An SQP Algorithm for Large-Scale Constrained Optimization,” *SIAM Rev.*, vol. 12, 2005.
- [11] R. H. Byrd, J. Nocedal, and R. A. Waltz, “KNITRO: An integrated package for nonlinear optimization,” in *Lrg. Scal. Nonlin. Opt.*, 2006.
- [12] A. Wächter and L. T. Biegler, “On the implementation of an interior-point filter line-search algorithm for large-scale nonlinear programming,” *Math. Progr.*, vol. 106, 2006.
- [13] “Harwell Subroutine Library, AEA Technology, Harwell, Oxfordshire, England. A catalogue of subroutines,” <http://www.hsl.rl.ac.uk/>.
- [14] C. Mastalli, J. Marti-Saumell, W. Merkt, J. Sola, N. Mansard, and S. Vijayakumar, “A Feasibility-Driven Approach to Control-Limited DDP,” *Autom. Rob.*, vol. 46, 2022.
- [15] F. Dellaert and M. Kaess, *Factor Graphs for Robot Perception*. Now Foundations and Trends, 2017.
- [16] R. Hartley, J. Mangelson, L. Gan, M. Ghaffari Jadidi, J. M. Walls, R. M. Eustice, and J. W. Grizzle, “Legged Robot State-Estimation Through Combined Forward Kinematic and Preintegrated Contact Factors,” in *IEEE Int. Conf. Rob. Autom. (ICRA)*, 2018.
- [17] V. Agrawal, S. Bertrand, R. Griffin, and F. Dellaert, “Proprioceptive State Estimation of Legged Robots with Kinematic Chain Modeling,” in *IEEE Int. Conf. Hum. Rob. (ICHR)*, 2022.
- [18] R. E. Bellman, *The Theory of Dynamic Programming*. RAND Corporation, 1954.
- [19] M. Kobilarov, D.-N. Ta, and F. Dellaert, “Differential dynamic programming for optimal estimation,” in *IEEE Int. Conf. Rob. Autom. (ICRA)*, 2015.
- [20] A. Oshin, M. D. Houghton, M. J. Acheson, I. M. Gregory, and E. A. Theodorou, “Parameterized Differential Dynamic Programming,” in *Rob.: Sci. Sys. (RSS)*, 2022.
- [21] C. Mastalli, S. P. Chhatoi, T. Corbères, S. Tonneau, and S. Vijayakumar, “Inverse-Dynamics MPC via Nullspace Resolution,” *IEEE Trans. Rob. (T-RO)*, vol. 39, 2023.
- [22] H. Li, W. Yu, T. Zhang, and P. M. Wensing, “A Unified Perspective on Multiple Shooting In Differential Dynamic Programming,” in *IEEE/RSJ Int. Conf. Intell. Rob. Sys. (IROS)*, 2023.
- [23] C. G. Atkeson, C. H. An, and J. M. Hollerbach, “Estimation of Inertial Parameters of Manipulator Loads and Links,” *The Int. J. of Rob. Res. (IJRR)*, vol. 5, 1986.
- [24] J. Carpentier and N. Mansard, “Analytical derivatives of rigid body dynamics algorithms,” in *Rob.: Sci. Sys. (RSS)*, 2018.
- [25] S. Singh, R. P. Russell, and P. M. Wensing, “Efficient Analytical Derivatives of Rigid-Body Dynamics Using Spatial Vector Algebra,” *IEEE Rob. Autom. Lett. (RA-L)*, vol. 7, 2022.
- [26] R. Featherstone, *Rigid body dynamics algorithms*. Springer, 2014.
- [27] S. Traversaro, S. Brossette, A. Escande, and F. Nori, “Identification of fully physical consistent inertial parameters using optimization on manifolds,” in *IEEE/RSJ Int. Conf. Intell. Rob. Sys. (IROS)*, 2016.
- [28] C. Rucker and P. M. Wensing, “Smooth Parameterization of Rigid-Body Inertia,” *IEEE Rob. Autom. Lett. (RA-L)*, vol. 7, 2022.
- [29] C. Mastalli, W. Merkt, G. Xin, J. Shim, M. Mistry, I. Havoutis, and S. Vijayakumar, “Agile maneuvers in legged robots: a predictive control approach,” *arXiv preprint arXiv:2203.07554*, 2022.
- [30] R. Budhiraja, J. Carpentier, C. Mastalli, and N. Mansard, “Differential Dynamic Programming for Multi-Phase Rigid Contact Dynamics,” in *IEEE Int. Conf. Hum. Rob. (ICHR)*, 2018.
- [31] P. M. Wensing, S. Kim, and J.-J. E. Slotine, “Linear Matrix Inequalities for Physically Consistent Inertial Parameter Identification: A Statistical Perspective on the Mass Distribution,” *IEEE Rob. Autom. Lett. (RA-L)*, vol. 3, 2017.
- [32] S. Martinez, R. Griffin, and C. Mastalli, “Derivations of multiple shooting optimal estimation algorithm,” 2024.
- [33] G. Frison, D. Kouzoupis, J. B. Jørgensen, and M. Diehl, “An efficient implementation of partial condensing for Nonlinear Model Predictive Control,” in *IEEE Conf. on Dec. Cntrl. (CDC)*, 2016.
- [34] J. Nocedal and S. Wright, *Numerical Optimization*, 2nd ed. New York, USA: Springer, 2006.
- [35] M. F. Fallón, M. Antone, N. Roy, and S. Teller, “Drift-free humanoid state estimation fusing kinematic, inertial and LIDAR sensing,” in *IEEE Int. Conf. Hum. Rob. (ICHR)*, 2014.